Nano Energy 80 (2021) 105506

Contents lists available at ScienceDirect

Nano Energy

journal homepage: http://www.elsevier.com/locate/nanoen

Full paper

Yolk-shell structured $CuSi_2P_3$@Graphene nanocomposite anode for long-life and high-rate lithium-ion batteries

Wenwu Li [a,b,*], Qibin Ma [b], Pengfei Shen [b], Yucun Zhou [a], Luke Soule [a], Yunyong Li [b], Yanxue Wu [b], Haiyan Zhang [b], Meilin Liu [a,*]

[a] School of Materials Science & Engineering, Georgia Institute of Technology, Atlanta, GA 30332, USA
[b] School of Materials and Energy, Guangdong University of Technology, Guangzhou 510006, PR China

ARTICLE INFO

Keywords:
Ternary phosphide
$CuSi_2P_3$
High-performance
Anodes
Li-ion batteries

ABSTRACT

Silicon-based anode materials enable the development of commercial lithium-ion batteries (LIBs) with higher gravimetric energy densities than are currently available. However, the inherently low electronic and ionic conductivity as well as large volume expansion upon lithiation of Si hinder their use in practical applications. Here we report a cation-disordered $CuSi_2P_3$ material, synthesized using high-energy ball milling, that shows improved stability, larger capacity, and higher ionic and electronic conductivity than pure Si. When used as an anode for LIBs, $CuSi_2P_3$ demonstrates a high reversible capacity of 2069 mA h g^{-1} with an initial Coulombic efficiency of 91% and a suitable working potential of 0.5 V (vs. Li^+/Li). Further, after a two-step ball milling of $CuSi_2P_3$ with graphite, a yolk-shell structured carbon-coated $CuSi_2P_3$@graphene nanocomposite is formed that shows enhanced long-term cycling stability (1394 mA h g^{-1} after 1500 cycles at 2 A g^{-1}; 1804 mA h g^{-1} after 500 cycles at 200 mA g^{-1}) and rate capability (530 mA h g^{-1} at 50 A g^{-1}), surpassing those for other Cu-Si, Cu-P, and Si-P compounds or single-component Si- and P-based composites. When coupled with a $LiNi_{0.5}Co_{0.2}Mn_{0.3}O_2$ (NCM) cathode in a full cell, the NCM//$CuSi_2P_3$ @graphene battery exhibits a high capacity of 140 mA h g^{-1} after 200 cycles, demonstrating the potential of $CuSi_2P_3$ anodes for the next-generation high-performance LIBs.

1. Introduction

Lithium-ion batteries (LIBs) of high gravimetric and volumetric energy and power densities are urgently needed for portable electronics and electric vehicles. In order to further expand into other markets, such as stationary energy storage of renewables and larger vehicles beyond cars, batteries must be made with higher gravimetric energy densities than are currently available. Silicon is one of the most promising anode materials to improve the gravimetric energy density of the next generation of LIBs [1–5]. While Si is inexpensive and offers a theoretical capacity of 4200 mA h g^{-1}, the low electronic and ionic conductivity as well as large volumetric change upon lithation (>300%) significantly hampers the practical applications of silicon anodes. To address the volume change, many efforts have been devoted to designing various nanostructures [6]. Among them, the yolk-shell structured silicon@carbon nanocomposite can effectively buffer the volume expansion while enhancing the electron transfer kinetics by offering a conductive pathway [7–12]. To obtain even higher electronic conductivity and stability, MXenes or graphene can be used to form Si binary or ternary nanocomposites [13]. Recently, Yin et al. synthesized a MXene-Si composite that showed higher rate capability than pure Si or MXene electrodes [14,15].

In addition to using nanocomposites, elemental doping and atomic substitution can be used to alter the inherent electronic and ionic conductivity and mechanical properties of Si anodes [16–19]. Typically, elements like B, Al, N, P, and S are used as dopants to enhance electronic or ionic conductivity [20–22]. However, only limited enhancement can be achieved with low doping level (<2%). $Si_{1-x}Ge_x$ ($0 < x < 1$) solid solutions offer improved performance [23–26] but are limited by the high cost of Ge.

To enhance the electronic and ionic conductivity and lower the volume change during lithiation, the current work combines Si with Cu and P to form the ternary compound $CuSi_2P_3$ using high-energy ball milling. The material has a cation-disordered cubic ZnS crystal structure, as determined from XRD refinement, and should have metallic behavior (no bandgap), according to DOS calculations. When used as an anode for

* Corresponding authors.
E-mail addresses: wenwuli@hust.edu.cn (W. Li), meilin.liu@mse.gatech.edu (M. Liu).

https://doi.org/10.1016/j.nanoen.2020.105506
Received 27 February 2020; Received in revised form 12 July 2020; Accepted 13 October 2020
Available online 20 October 2020

LIBs, the material delivers a high reversible capacity of 2069 mA h g^{-1} with a suitable working potential of 0.5 V and an initial Coulombic efficiency up to 91%. Ex-situ XRD and HRTEM along with SAED, Raman and XPS analyses confirm that $CuSi_2P_3$ experiences a reversible two-stage Li-storage mechanism with both intercalation and conversion reactions. When combined with graphite in a two-step ball milling process, a yolk-shell structured carbon coated $CuSi_2P_3$@graphene nanocomposite is formed that demonstrates a suitable cycling stability (1394 mA h g^{-1} after 1500 cycles at 2 A g^{-1} and 1804 mA h g^{-1} after 500 cycles at 200 mA g^{-1}); and rate capability (530 mA h g^{-1} at 50 A g^{-1}), that surpasses the performances of most related binary and single-component anodes reported previously. A full cell consisting of $LiNi_{0.5}Co_{0.2}Mn_{0.3}O_2$ cathode and $CuSi_2P_3$@C anode maintain a reversible capacity of 140 mA h g^{-1} after 200 cycles, implying that the $CuSi_2P_3$@C is a promising anode for high-performance LIBs.

2. Experimental section

2.1. Material synthesis

The raw materials of Cu, Si, and red P powders were used as received. To obtain a high impact energy, stainless steel grinding tanks with a volume of 500 mL and grinding balls with a diameter of 10 mm were used. The mixture of Cu, Si, and red P in a molar ratio of 1:2:3 was added into the tanks filled with argon. The mass ratio of raw materials to steel balls was 1:25. 3 g powder was ball milled for each run by the planetary mono mill (Fritsch Pulverisette-6) at a speed of 300 rpm for 7 h, with a duration time of 10 mins and a rest time of 5 mins. To obtain a better mechanical alloying, a reverse operation mode (regular reversal of the direction of rotation) was adopted. To prepare the yolk-shell structured $CuSi_2P_3$@graphene nanocomposite, graphite was added into the as-prepared $CuSi_2P_3$ with a weight ratio of 1:7 (graphite:$CuSi_2P_3$) and ball milled at 400 rpm for 20 h. Then the as-synthesized carbon-coated $CuSi_2P_3$ was further mixed with additional graphite in a weight ratio of 1:8 and milled at 200 rpm for another 30 mins to produce yolk-shell structured carbon coated $CuSi_2P_3$@graphene nanocomposites. Other controlled experiments illustrated in the text were performed in a similar method.

2.2. Material characterization

The as-synthesized powder samples were characterized by X-ray diffraction (XRD, Bruker D8 ADVANCE) using CuKα radiation at a scanning speed of 1° min^{-1} and the Confocal Raman spectrometer (Raman, WTEC ALPHA300 with a 325 nm excitation laser). The morphology and microstructure of the samples were characterized using a field-emission scanning electron microscope (FESEM, Hitach SU8220) and field-emission transmission electron microscope (TEM, FEI, Thermo Talos F200S). The related samples were also characterized by X-ray photoelectron spectroscopy (XPS Thermo Fisher Escalab 250Xi using Al Kα radiation).

2.3. Electrochemical characterization

For the pure phase $CuSi_2P_3$, the electrode films were prepared by coating the slurry of 70 wt% $CuSi_2P_3$, 20 wt% carbon black and 10 wt% Li-PAA binder onto the copper foil and dried in vacuum oven at 100 °C for overnight. For the $CuSi_2P_3$@graphene nanocomposite, the electrode films were prepared by coating the slurry of 90 wt% $CuSi_2P_3$@ few layered graphene nanocomposite, and 10 wt% binder onto the copper foil without any extra conducting agents. The electrochemical characterizations were conducted by utilizing CR2032 coin cells assembled in an Ar-filled glovebox (H_2O <0.02 ppm, O_2 <0.02 ppm, Mbraun, Labmaster 130). Li foils were used as counter and reference electrodes, and 1 M $LiPF_6$ in ethylene carbonate/diethylene carbonate (EC/DEC, 1 : 1 vol%) was used as the electrolyte. The loading of the active material on the Cu foil is controlled within the range of 1.5–2 mg cm^{-2}. When assembling the $LiNi_{0.5}Co_{0.2}Mn_{0.3}O_2$//$CuSi_2P_3$@graphene nanocomposite battery, anode capacity is about 1.2 times larger than cathode. Galvanostatic discharge/charge tests were conducted on a LAND battery tester (Wuhan Kingnuo Electronic Co., China) and a testing system (Hokuto Denko, HJ1001SD8). The gravimetric specific capacity was evaluated based on the mass of reactive materials. Cyclic voltammetric (CVs) measurements were conducted on an electrochemical workstation (Autolab, Pgstat 302 N). The $LiNi_{0.5}Co_{0.2}Mn_{0.3}O_2$ applied in full cells is commercially available.

2.4. Computational details

The first-principles calculations were carried out by utilizing VASP (Vienna Ab-initio Simulation Package) [27,28]. We applied the exchange correlation functional with generalized gradient approximation proposed by Perdew, Burke and Ernzerhof. The core-electrons were held frozen by virtue of projector augmented wavefunction, with valence electron configuration for Cu $3d^{10}4\ s^1$, Si $3\ s^2 3p^2$, and P $3\ s^2 3p^3$. We applied the 4×4x4 Monkhorst-Pack reciprocal grid, together with 400 eV energy cutoff as sufficient energy calculations. We also utilized Gaussian smearing with a smearing width of 0.05 eV to accelerate computation of the electronic energy near Fermi level.

3. Results and discussion

The Si_xGe_{1-x} solid solutions ($0 < x < 1$) with a diamond-like crystal structure [23–26] have an enhanced Li-storage performance, compared with single-component Si or Ge electrodes. Actually, elements with a larger range of valences and various ratios can also be combined into the similar crystal structure, e.g., $A^{II}B^{IV}C_2^{\ V}$ and $A^{I}B_2^{IV}C_3^{V}$. Here, we successfully prepared $CuSi_2P_3$ by virtue of a facile and scalable ball milling method at ambient temperature and pressure, thus avoiding the conventional high-temperature chemical vapor transportation technique [29–31]. To study the synthesis process, XRD patterns of the powders with increasing ball milling time were collected. Seen in Fig. S1, peaks associated with the precursor materials (Cu, Si, and amorphous red P) is still seen after 1 h. After 3 h of milling, binary Cu-P phases (e.g., Cu_3P and CuP_2) were formed and Si and amorphous P remained. The formation priority of Cu-P intermediate compounds instead of Si-P or Cu-Si compounds can be attributed to the superiority in thermodynamic stability of Cu-P compounds. Beyond 7 h of milling, all peaks associated with the precursor powders disappeared and the new evolved ones seem to be of Si but all shifted to a higher angle, suggesting that a new ternary compound was formed with the composition of $CuSi_2P_3$. To characterize the crystal structure of the newly formed phase, we performed XRD refinement of the pattern (Fig. 1a). More crystallographic details are provided in Table S1-Table S2. The unit cell can be indexed to a cation-disordered cubic ZnS crystal structure, where Cu and Si atoms randomly occupy Zn sites in a 1:2 stoichiometric ratio and P replaces the S site. The crystal structure is depicted in Fig. 1b. To validate the proposed structure model, selected area electron diffraction (SAED, Fig. 1c) and high-resolution TEM (HRTEM, Fig. 1d) were performed. The ring-like diffraction pattern is attributed to the cubic ZnS crystal structure. No additional rings related to a cation-ordered superstructure were present. The observed (220) and ($2\bar{2}0$) crystal planes along the [001] zone axis further confirm the cation-disordered cubic ZnS structure. The lack of cation ordering is attributed to: 1) the high-temperature, high-pressure, and fast cooling rates associated with the high energy mechanical ball milling process; 2) the similar atomic radius and electronegativity of Cu and Si; 3) the formation of nanoparticles (Fig. 1a) [32,33]. To gain incite into local atomic structure, Raman spectroscopy was performed. As seen in Fig. 1e, the characteristic Raman spectra of the as-obtained $CuSi_2P_3$ is different from those of the Si and milled P counterparts. This means that the local bonding is different, further providing evidence for the

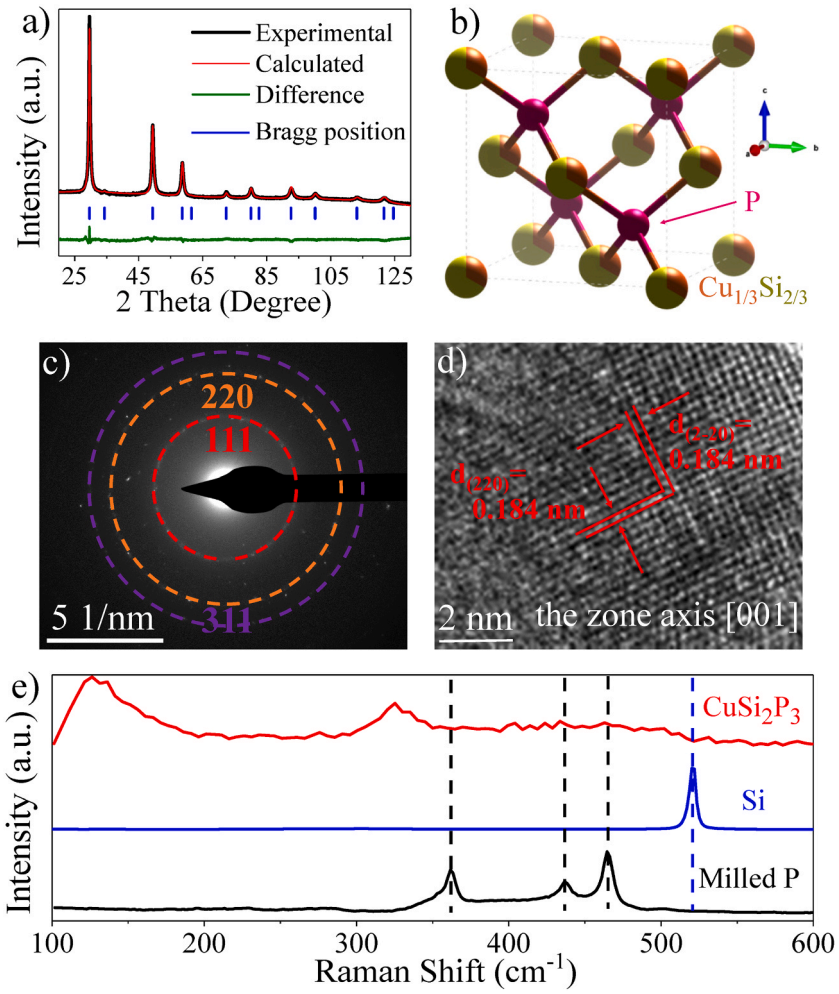

Fig. 1. a) XRD refinement of the as-obtained $CuSi_2P_3$ powder; b) schematic cation-disordered crystal structure of $CuSi_2P_3$; c) selected area electron diffraction (SAED) of the as-obtained $CuSi_2P_3$ powder; d) high-resolution transmission electron microscopy (HRTEM) of the as-obtained $CuSi_2P_3$ powder; e) Raman spectroscopy of the as-obtained $CuSi_2P_3$ powder, milled P and Si powder.

formation of the new phase. In summary, we successfully synthesized the cation-disordered Si-like ternary $CuSi_2P_3$. The cation-disordered structure has a higher symmetry, thus favoring Li^+-storage due to the reduced bandgap and lower Li-ion diffusion energy barrier and better strain accommodation, compared with the cation-ordered one [34–36].

Inspired by the cation-disordered Si-like crystal structure and binary Li-reactive components of Si and P, we prognosticated that the as-obtained $CuSi_2P_3$ compound would demonstrate its unique electrochemical Li-storage behavioral features, compared with the intermediate mixtures obtained during the ball milling process. The milled precursors at 1 h and 3 h were used as a performance reference. The initial discharge/charge profiles of the materials cycled at a current density of 200 mA g^{-1} are shown in Fig. 2a. It can be seen that pure $CuSi_2P_3$ has a higher initial Coulombic efficiency (91%) and smaller polarization than the intermediate mixtures. The multi-stage plateaus associated with the Cu+ 2Si+ 3 P @ 3 h electrode can be attributed to the hybridized electrochemical Li-storage features of the mixed phases of $CuSi_2P_3$, CuP_2, Cu_3P, and residual raw materials of Si and P, as characterized by XRD shown in Fig. S1 [37]. As seen in Fig. 2b, the peaks in the cyclic voltammetry scans of the first three cycles of the $CuSi_2P_3$ compound (inset) are consistent with the working potential plateaus showed in the initial three discharge/charge profiles (Fig. 2b). During the first discharge, there is a reduction peak at 0.22 V (vs. Li^+/Li) that can be attributed to the initial reaction with Li and minor side reaction such as solid electrolyte interphase. During the first charge, three oxidation peaks located at 0.46 V, 0.72 V, and 1.15 V are present that correspond to the release of Li from Li-Si, Li-P, and $Li_xCuSi_2P_3$, respectively. The second cycle shows two reduction peaks at 0.76 V, and 0.32 V that can be attributed to $Li_xCuSi_2P_3$ and Li-P as well as Li-Si reactions, respectively. Compared with the initial cycle, the lower overpotential in the subsequent cycles can likely be attributed to defects formed during the first discharge/charge process [38,39]. As seen in Fig. 2c, $CuSi_2P_3$ maintains a capacity of 1950 mA h g^{-1} at 200 mA g^{-1} after 30 cycles, which is higher than that of the ball-milled precursors. In the rate performance plot in Fig. 2d, it is seen that the material has a notable capacity of 220 mA h g^{-1} at a current rate of 20 A g^{-1}, much better than the intermediate counterparts. The improved rate performance is likely due to the high electrical conductivity of the compound. When pure $CuSi_2P_3$ was used as an electrode without addition of any carbon additive, the cell still delivered a large capacity (over 1500 mA h g^{-1} at 200 mA g^{-1}), high initial Coulombic Efficiency (greater than 90%), and suitable working potential of 0.5 V (Fig. S2).

Electron and Li-ion transport properties are of vital importance to electrochemical Li-storage performance for a new electrode material. To qualify the electronic conductivity of the cation-disordered $CuSi_2P_3$, electrochemical impedance spectroscopy (EIS) was performed (Fig. 3a). The observed charge transfer resistance (Rct, Fig. 3b) of the cell using $CuSi_2P_3$ is 84 Ω, which is smaller than that of the cells using ball-milled Si (729 Ω), suggesting that $CuSi_2P_3$ has much higher electrical conductivity. To explain the origin of electronic conductivity of the as-

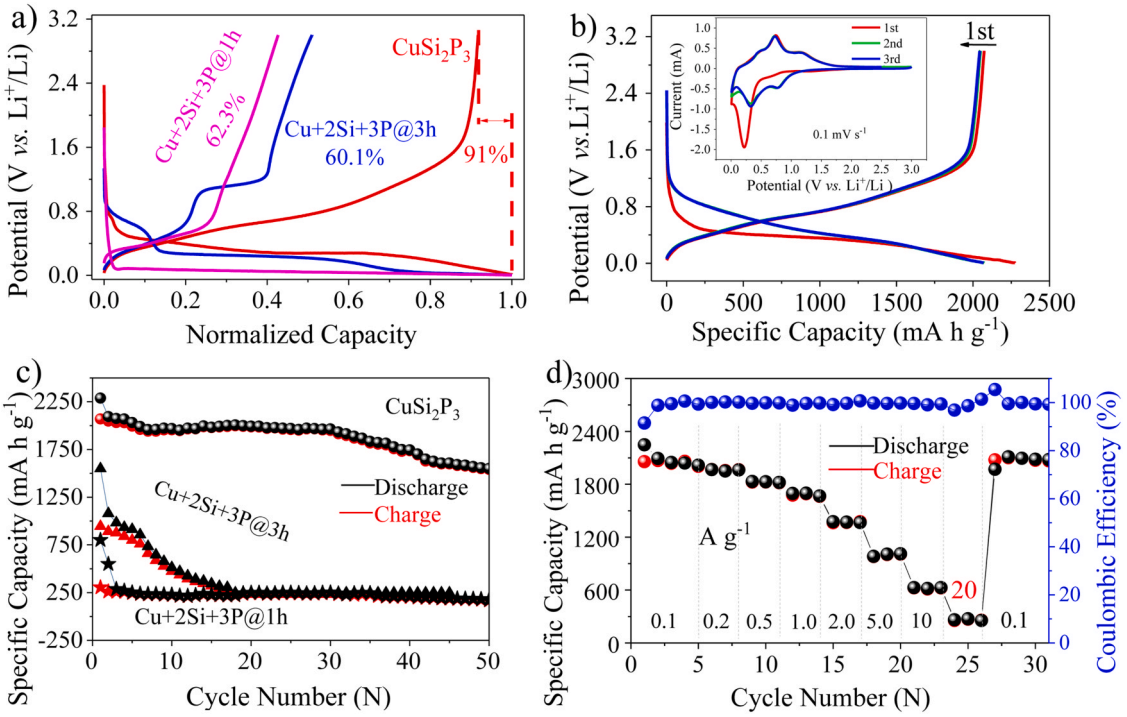

Fig. 2. a) initial discharge/charge profiles of the as-obtained $CuSi_2P_3$ and the intermediate ball milled products; b) initial three discharge/charge profiles and cyclic voltammetry curves (the inset) of the as-obtained $CuSi_2P_3$; c) cycling stability of the as-obtained $CuSi_2P_3$ and the ball milled intermediate products; d) rate performance of the as-obtained $CuSi_2P_3$.

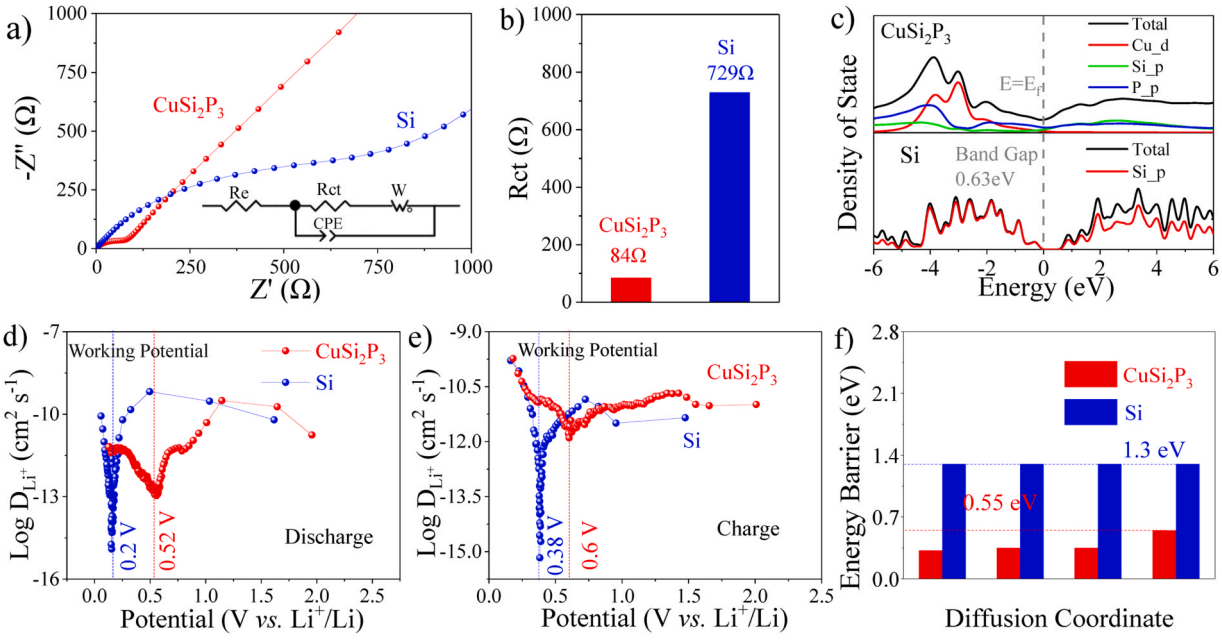

Fig. 3. a) electrochemical impedance spectroscopy of the cell with $CuSi_2P_3$/Si electrodes; b) the charge transfer resistance (Rct) obtained from the a); c) calculated density of state (DOS) of the cation-disordered $CuSi_2P_3$ and Si. d,e) Li-ion diffusion coefficients of the cation-disordered $CuSi_2P_3$ and Si during discharge and charge; f) calculated Li-ion diffusion energy barrier of $CuSi_2P_3$ and Si.

synthesized $CuSi_2P_3$, we assorted to first-principle calculations to predict the electronic structure of the material. The total density of state (DOS) of $CuSi_2P_3$ is shown in Fig. 3c. Clearly, the material has no bandgap (its total DOS crosses the Fermi level), offering evidence for its metallic conductivity. This is consistent with the experimental results. The metallic conductivity of $CuSi_2P_3$ is originated from the co-contribution of the p bands of P and Si elements and the d band of Cu element as compared in partial density of state of Cu, Si and P elements in the cation-disordered $CuSi_2P_3$ (Fig. 3c). As a comparison, we have also calculated the total DOS of pure Si. Its total DOS value is zero at Fermi level, suggesting its semiconductor feature (Fig. 3c, bottom). To qualify the Li^+ diffusivity of the cation-disordered $CuSi_2P_3$, the galvanostatic intermittent titration technique (GITT) was used. Li^+ diffusion coefficient is obtained on the basis of the following equation[40,41]:

$$D = \frac{4}{\pi\tau}\left(\frac{n_m V_m}{A}\right)^2\left(\frac{\Delta E_s}{\Delta E_\tau}\right)^2$$

where D denotes Li^+ diffusion coefficient ($cm^2\ s^{-1}$), τ means duration of the current pulse (s), n_m stands for the number of moles of active material (mol), V_m represents molar volume of the electrode ($cm^3\ mol^{-1}$), A is contact area between electrode and electrolyte (cm^2, in this case the surface area is the real area of the current collector), ΔE_s is the steady-state voltage change owing to the current pulse (V), and ΔE_τ corresponds to the voltage change during the constant current pulse neglecting the IR drop (V). As shown in Fig. 3d, e and Fig. S3, the obtained Li-ion diffusion coefficient of the $CuSi_2P_3$ at the working potential is three to four orders of magnitude larger than that of the ball milled Si. According to the DFT calculations, the Li-ion diffusion energy barriers of $CuSi_2P_3$ are less than 0.55 eV, much smaller than that (1.3 eV) of the ball miled Si electrode (Fig. 3f). The theoretical Li-ion diffusion paths used for calculations are provided in Fig. S4 and S5. Additionally, the faster Li-ion diffusivity can be attributed to the lower elastic modulus, which means the softer mechanical property compared with Si counterpart, as shown in Fig. S6.

To investigate the Li-storage mechanism of $CuSi_2P_3$, we performed ex-situ XRD, XPS, Raman and HRTEM along with SAED measurements. Typical discharge and charge profiles of the Li-$CuSi_2P_3$ cell with marked working potentials for XRD measurements are shown in Fig. 4a. As the cell was discharged, the peak intensities significantly decrease, likely implying amorphization or reduced particle size. Specifically, the initial discharge stage (from Figure $4b_1$ to Figure $4b_2$, and Fig. S7) involves peaks shift towards lower two-theta, indicative of a lattice expansion after the Li-ion insertion into the voids of the $CuSi_2P_3$. A schematic of this Li-inserted lattice is shown in Fig. S8. To calculate the contribution to the overall capacity of this initial Li-insertion, we can assum Li fills all the tetrahedral interstitial sites (Fig. S8) of $CuSi_2P_3$. Since there are three such sites, $CuSi_2P_3$ can at most host three Li-ions, forming the compound $Li_3CuSi_2P_3$ that results in an intercalation capacity of 379 mA h g^{-1}. This value is almost consistent with the observed capacity as marked in Fig. 4a. As more lithium is inserted, the structure amorphized and the diffraction peaks disappear (Figure $4b_3$). The corresponding HRTEM images show no features during this stage (Fig. S9-iii), further confirming the amorphization. As more Li is inserted into the amorphous phase, the saturated Li-contained amorphous electrode began to

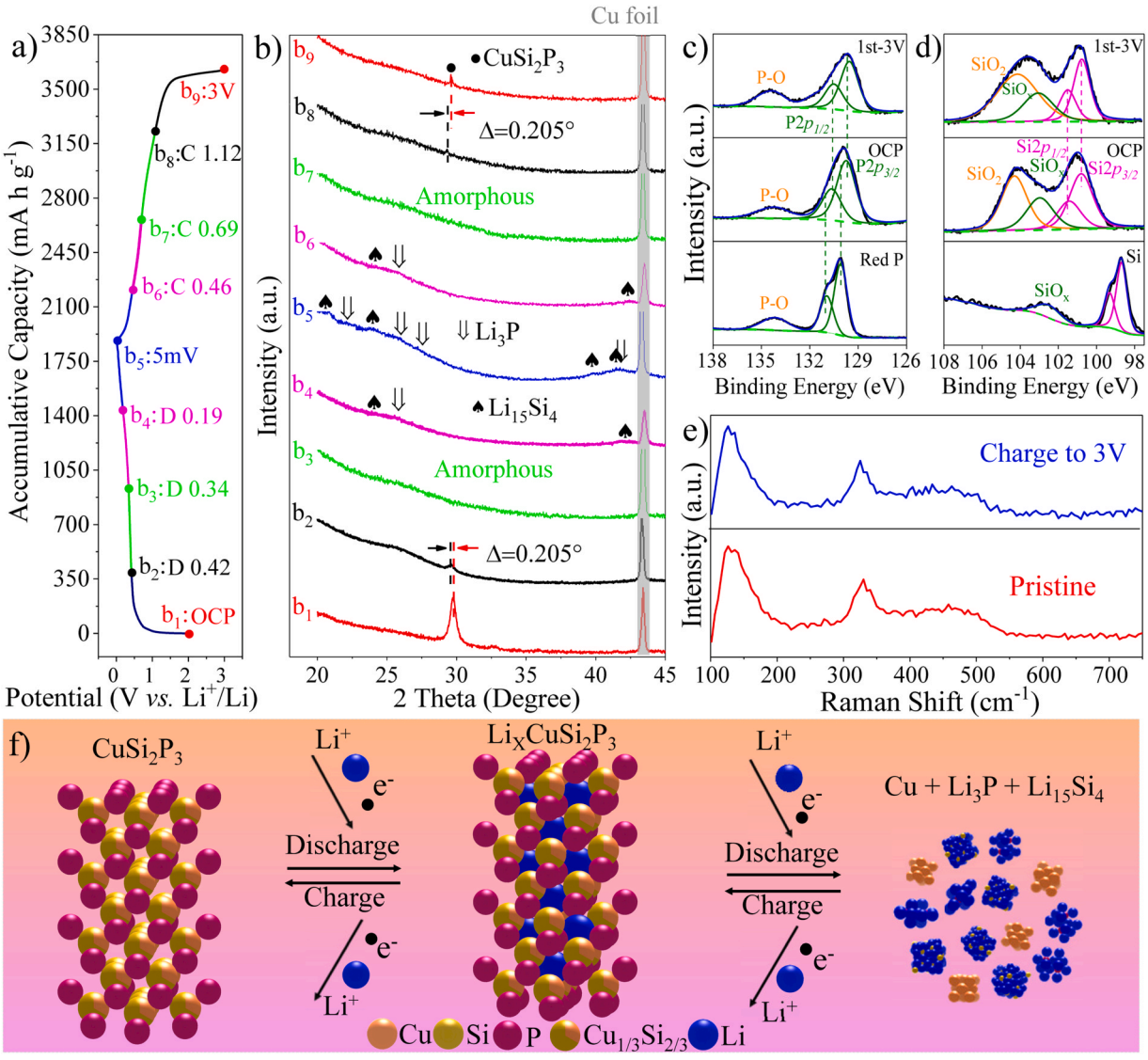

Fig. 4. The Li^+-storage mechanisms characterizations of the as-prepared cation-mixed $CuSi_2P_3$ anodes: a) first discharge/charge curves for the ex-situ characterizations at 200 mA g^{-1}; b) ex-situ XRD patterns corresponded to indicators marked in a). High-resolution XPS spectra of $CuSi_2P_3$ electrode after initial cycling, pristine $CuSi_2P_3$ powder and raw material of Si or P: c) P 2p; d) Si 2p. e) Raman spectra of $CuSi_2P_3$ electrode after initial cycling and pristine $CuSi_2P_3$ powder; f) schematic Li^+-storage process.

separate into the binary lithium alloys of Li_3P and $Li_{3.75}Si$ (Figure 4b$_4$, 4b$_5$ and HRTEM along with FFTs in Fig. S9-vi, S10). During the charge process, the binary Li-M (M=Si, and P) phases disappear and the material becomes entirely amorphous once again as shown in Figure 4b$_7$ and Fig. S9-vii. When fully charged to 3.0 V, the diffraction pattern of the as-synthesized $CuSi_2P_3$ reappears, which suggests a reversible Li-storage process (Figure 4b$_9$ and Fig. S9-ix). To validate this reversibility, we further performed ex-situ XPS and Raman measurements. Compared with the signals of the precursors and pristine $CuSi_2P_3$, the signature of the as-synthesized $CuSi_2P_3$ reappears after cycling, validating the high reversibility of the $CuSi_2P_3$ anode (Fig. 4c, d and e). The Li^+-storage mechanisms of the $CuSi_2P_3$ electrode is depicted schematically in Fig. 4f and is expressed in the following equations:

During discharge:

$$CuSi_2P_3 + xLi^+ + xe^- \rightarrow Li_xCuSi_2P_3 \quad (x<3); \tag{i}$$

$$Li_xCuSi_2P_3 + (16.5-x)Li^+ + (16.5-x)e^- \rightarrow Cu + 2\ Li_{3.75}Si + 3\ Li_3P; \tag{ii}$$

During charge:

$$2\ Li_{3.75}Si + Cu + 3\ Li_3P - (16.5-x)Li^+ - (16.5-x)e^- \rightarrow Li_xCuSi_2P_3; \tag{iii}$$

$$Li_xCuSi_2P_3 - x\ Li^+ - x\ e^- \rightarrow CuSi_2P_3; \tag{iv}$$

$$\text{Overall reaction}: CuSi_2P_3 + 16.5Li^+ + 16.5e^- \leftrightarrow Cu + 2\ Li_{3.75}Si + 3\ Li_3P. \tag{v}$$

Based on this proposed mechanism, the $CuSi_2P_3$ electrode can uptake 16.5 Li-ions per formula unit, corresponding to a theoretical specific capacity of 2079 mA h g^{-1} in which the two Si atoms deliver a capacity of 945 mA h g^{-1}, and three P atoms deliver a capacity of 1134 mA h g^{-1}. Unreacted Cu atoms can provide enhanced electronic conductivity and a physical barrier against agglomeration. The initial-cycle capacity was found to be 2069 mA h g^{-1}, which is consistent with the calculated theoretical value based on Equation V, validating the rationality of the above reaction mechanism.

To further enhance the cycling stability and rate performance of the $CuSi_2P_3$ anode, the material was carbon coated using a two-step ball milling method with graphite. The resulting material resembled a yolk-shell morphology, with amorphous-carbon-coated $CuSi_2P_3$ particles appearing to be covered in several layers of graphene. The synthesis process is schematically depicted in Fig. 5a. After the first high-energy ball milling step for 20 h, the carbon coating appeared to be amorphous and the $CuSi_2P_3$ is also refined into less than 5 nm, as seen from the inset HRTEM in Fig. 5a. The formed amorphous carbon and ultrafine or amorphous $CuSi_2P_3$ aggregations can be attributed to the durable high-energy mechanical ball milling, which produced enough energy to grind the lab-synthesized $CuSi_2P_3$ and destroy the layered graphite into

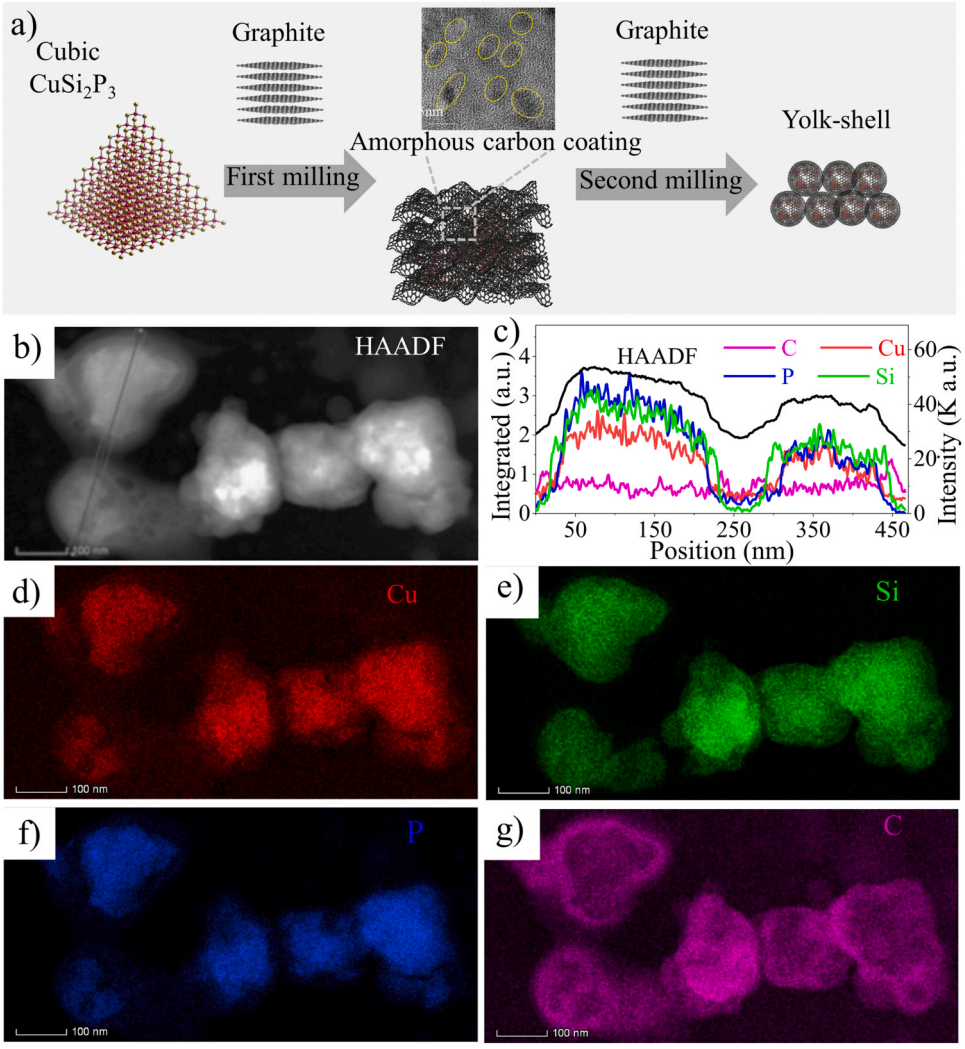

Fig. 5. a) Schematic two-stage ball milling processes. b) low-magnification TEM image of yolk-shell-structured $CuSi_2P_3$@graphene nanocomposite. c) line scan data as indicated in b). d-g) elemental mapping of the obtained carbon coating $CuSi_2P_3$@graphene nanocomposite.

amorphous carbon. The final nanocomposite was formed via a second short-time ball milling at 200 rpm for 0.5 h. The formation of a graphene shell from the second-added graphite can be attributed to mechanical exfoliation by shear forces during the mechanical milling process [42–44]. Fig. 5b, Fig. S11 and Fig. S12 show the low-magnitude TEM and FSEM images of the yolk-shell structured carbon-coated $CuSi_2P_3$@graphene nanocomposite. The carbon shell is shown clearly through an elemental line scan and mapping image (Fig. 5c-g, and Fig. S11a-e, S13). And the graphene can be confirmed by the HRTEM (Fig. S11-f) image on the carbon shell via the measured D-spacing of 0.32–0.34 nm.[45,46] The graphene is about 3–9 layers. The ratio of $CuSi_2P_3$ to carbon in the final material was also determined to be close to 7:2 by the thermal gravimetric analysis shown in Fig. S14, which is well consistent with the poured amount of $CuSi_2P_3$ and graphite. The

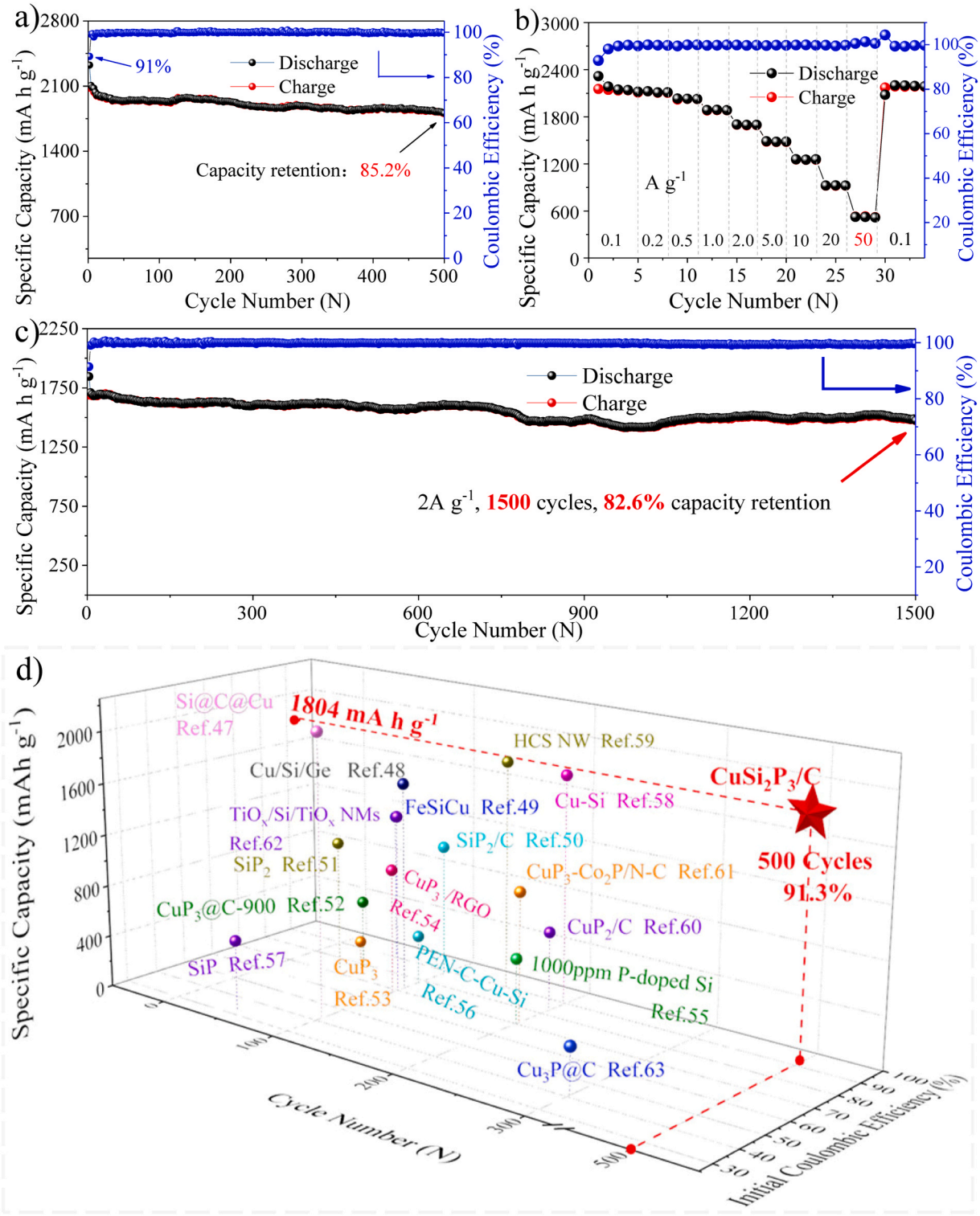

Fig. 6. Electrochemical performance of the $CuSi_2P_3$@graphene nanocomposite: a) cycling stability at 0.2 A g^{-1}; b) rate performance; c) cycling stability at 2 A g^{-1}; and d) performance comparison of $CuSi_2P_3$@graphene nanocomposite with recently reported P-based and Si-based anodes in terms of initial Coulombic efficiency, and cycling stability.

amorphous carbon along with few layered graphene can not only buffer the volume expansion but also promote the Li-ion and electron transportation of $CuSi_2P_3$. In addition, such a morphology is also favorable when applied to batteries. On one hand, the small primary nanoparticles can enhance the intimate contact between the active materials and the electrolyte, thus reducing the lithium-ion diffusion length and increasing the rate capability. On the other hand, the large (micro-sized) secondary particles can increase the electrode density and hence the volumetric energy density.

Performance of the cation-disordered $CuSi_2P_3$ was significantly enhanced by the bilayer carbon coating. As seen in Fig. 6a, the yolk-shell structured carbon-coated $CuSi_2P_3$@graphene nanocomposite delivered a high capacity of 1804 mA h g^{-1} after 500 cycles at a current density of 200 mA g^{-1} within the working potential varying from 3.0 V to 0.005 V, which is improved over the uncoated sample. The superior cycling stability can be attributed to the effective carbon buffer matrix to accommodate the volume change during Li-ion uptake/release process. The rate performance is shown in Fig. 6b. The nanocomposite delivered capacities of 2143, 2106, 2010, 1880, 1690, 1480, 1252, and 922 mA h g^{-1}, at a current rate of 0.1, 0.2, 0.5, 1, 2, 5, 10, and 20 A g^{-1}, respectively. At a current density of 50 A g^{-1}, the capacity can be maintained at 530 mA h g^{-1}, above that of the pure sample. The excellent rate performance mainly benefits from the inherent metallic conductivity and fast Li-ion diffusion of $CuSi_2P_3$ as well as the further reduced particle size and the introduced few layered graphene. Regarding long-term stability, the nanocomposite can be cycled at 2 A g^{-1} with a reversible capacity of 1394 mA h g^{-1} for 1500 cycles, as seen in Fig. 6c. The performance of the nanocomposite in this work outperforms most reported binary Si-P, Cu-P and Cu-Si compounds as well as single-component Si-, and P-based composites in terms of cycling stability, and initial Coulombic efficiency, which are compared in Fig. 6d [47–63].

Considering the excellent Li-storage performance of the as-designed carbon-coated $CuSi_2P_3$@few layered graphene nanocomposite, we further evaluate the material in a realistic application. The $CuSi_2P_3$@graphene nanocomposite was coupled with a $LiNi_{0.5}Co_{0.2}Mn_{0.3}O_2$ cathode in full batteries[64–68]. In the first cycles, the full battery was activated at low current density. After the activation, its Coulombic efficiency is approaching to 100%. As shown in Fig. 7a, the typical discharge/charge profile of the $LiNi_{0.5}Co_{0.2}Mn_{0.3}O_2$//$CuSi_2P_3$@graphene nanocomposite full cell demonstrates a capacity of 140 mA h g^{-1} with an average working potential of 3.3 V based on the mass of the $LiNi_{0.5}Co_{0.2}Mn_{0.3}O_2$ cathode. The high output potential and smooth discharge/charge profile of the full cell can be attributed to the suitable electrochemical properties of the $CuSi_2P_3$@graphene anode. The potential curves of both anode and cathode are seen Fig. 7b. More importantly, despite the capacity decay in the initial 50 cycles, a stable cycling of the full cell was observed over 200 cycles (Fig. 7c), making $CuSi_2P_3$@graphene a promising anode for high-performance LIBs.

4. Conclusion

In summary, we have designed and successfully synthesized a ternary phosphide $CuSi_2P_3$ by a low-cost and scalable ball milling process. The as-prepared $CuSi_2P_3$ has a cation-disordered cubic ZnS structure with metallic behavior (no apparent bandgap), as predicted from theoretical calculations and confirmed by experimental measurements. When used as an anode for LIBs, $CuSi_2P_3$ delivered a reversible capacity of 2069 mA h g^{-1} with a working potential of ~0.5 V. The material exhbits a reversible Li^+-storage mechanism, as validated using ex-situ XRD, HRTEM, XPS, and Raman spectroscopy. When the $CuSi_2P_3$ was ball-milled with graphite, a yolk-shell structured $CuSi_2P_3$@graphene nanocomposite was formed that demonstrated enahnced Li^+-stroage performance in terms of cyclability and initial Coulombic efficiency. When combined with a $LiNi_{0.5}Co_{0.2}Mn_{0.3}O_2$ cathode in a full cell, a capacity of 140 mA h g^{-1} was maintained over 200 cycles. The enhancement in performance and stability of the $CuSi_2P_3$@graphene nanocomposite is attributed to the high electronic conductivity and Li^+

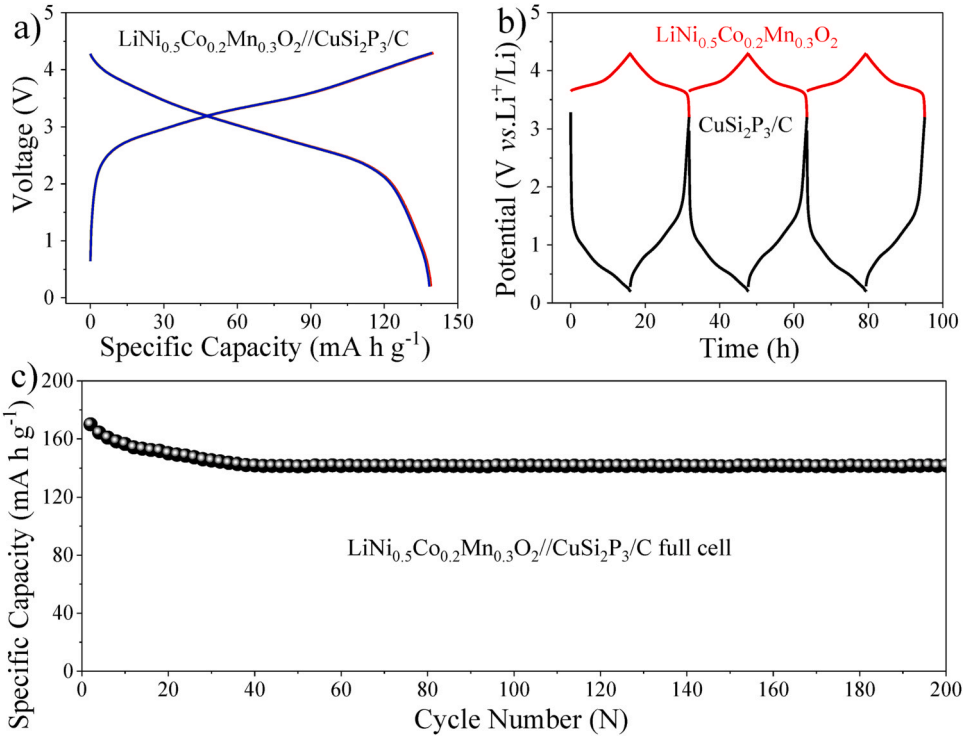

Fig. 7. a) typical discharge/charge profile of the $LiNi_{0.5}Co_{0.2}Mn_{0.3}O_2$//$CuSi_2P_3$@graphene nanocomposite full battery; b) typical discharge/charge profiles of the $LiNi_{0.5}Co_{0.2}Mn_{0.3}O_2$ cathode and the yolk-shell structured $CuSi_2P_3$@graphene anode; c) cycling stability of the assembled $LiNi_{0.5}Co_{0.2}Mn_{0.3}O_2$//$CuSi_2P_3$@graphene nanocomposite full battery at a current density of 100 mA g^{-1}.

diffusivity of $CuSi_2P_3$ and the buffered volume expansion by the graphene coating. This research offers important insight into rational design of new teranry Si-based anode materials for high-performance Li-ion batteries.

Supporting information

Additional details on crystallographic details, X-ray diffraction (XRD) patterns, galvanostatic discharge/charge curves, galvanostatic intermittent titration technique (GITT) curves, simulation models utilized for first-principles calculations, theoretical Li-ion diffusion paths calculations, total Elastic Moduli, TEM micrographs, crystal structure of $Li_3CuSi_2P_3$, ex-situ HRTEM images at different potentials, and elemental mapping.

CRediT authorship contribution statement

Wenwu Li: Supervision, Conceptualization, Investigation, Data curation, Calculating, Writing-original draft. **Qibin Ma:** Investigation, Data Curation. **Pengfei Shen:** Investigation, Software, Data Curation. **Yucun Zhou:** Writing - review & editing. **Luke P Soule:** Writing - review & editing. **Yunyong Li:** Resources, Formal analysis. **Yanxue Wu:** Data curation, Resources. **Haiyan Zhang:** Resources. **Meilin Liu:** Supervision, Conceptualization, Writing - review & editing, Visualization, Resources.

All authors discussed the results and contributed to the final manuscript.

Declaration of Competing Interest

The authors declare that they have no known competing financial interests or personal relationships that could have appeared to influence the work reported in this paper.

Acknowledgements

We acknowledge National Natural Science Foundation of China (21701030), Guangdong Province Natural Science Foundation (2017A030310241), Science and Technology Planning Project of Guangzhou City (201804010392), Guangdong Innovative and Entrepreneurial Research Team Program (No. 2014ZT05N200), US National Science Foundation (DMR-1742828). The authors acknowledge the utilization of facilities in Georgia Institute of Technology and Guangdong University of Technology. Computational work used resources of the National Energy Research Scientific Computing Center (NERSC), a U.S. Department of Energy Office of Science User Facility operated under Contract No. DE-AC02–05CH11231.

Appendix A. Supporting information

Supplementary data associated with this article can be found in the online version at doi:10.1016/j.nanoen.2020.105506.

References

[1] J. Wang, L. Liao, H.R. Lee, F. Shi, W. Huang, J. Zhao, A. Pei, J. Tang, X. Zheng, W. Chen, Y. Cui, Surface-engineered mesoporous silicon microparticles as high-Coulombic-efficiency anodes for lithium-ion batteries, Nano Energy 61 (2019) 404–410.
[2] H. Jia, J. Zheng, J. Song, L. Luo, R. Yi, L. Estevez, W. Zhao, R. Patel, X. Li, J.-G. Zhang, A novel approach to synthesize micrometer-sized porous silicon as a high performance anode for lithium-ion batteries, Nano Energy 50 (2018) 589–597.
[3] Z. Yan, J. Guo, High-performance silicon-carbon anode material via aerosol spray drying and magnesiothermic reduction, Nano Energy 63 (2019), 103845.
[4] Y. Shi, J. Wan, J.-Y. Li, X.-C. Hu, S.-Y. Lang, Z.-Z. Shen, G. Li, H.-J. Yan, K.-C. Jiang, Y. Guo, R. Wen, L.-J. Wan, Elucidating the interfacial evolution and anisotropic dynamics on silicon anodes in lithium-ion batteries, Nano Energy 61 (2019) 304–310.
[5] G. Li, J. Li, F.-S. Yue, Q. Xu, T.-T. Zuo, Y. Yin, Y.-G. Guo, Reducing the volume deformation of high capacity SiOx/G/C anode toward industrial application in high energy density lithium-ion batteries, Nano Energy 60 (2019) 485–492.
[6] Z. Liu, Q. Yu, Y. Zhao, R. He, M. Xu, S. Feng, S. Li, L. Zhou, L. Mai, Silicon oxides: a promising family of anode materials for lithium-ion batteries, Chem. Soc. Rev. 48 (2019) 285–309.
[7] L. Zhang, C. Wang, Y. Dou, N. Cheng, D. Cui, Y. Du, P. Liu, M. Al-Mamun, S. Zhang, H. Zhao, A yolk–shell structured silicon anode with superior conductivity and high tap density for full lithium-ion batteries, Angew. Chem. Int. Ed. 58 (2019) 8824–8828.
[8] J. Yang, Y.-X. Wang, S.-L. Chou, R. Zhang, Y. Xu, J. Fan, W.-X. Zhang, H.K. Liu, D. Zhao, S.X. Dou, Yolk-shell silicon-mesoporous carbon anode with compact solid electrolyte interphase film for superior lithium-ion batteries, Nano Energy 18 (2015) 133–142.
[9] N. Liu, J. Liu, D. Jia, Y. Huang, J. Luo, X. Mamat, Y. Yu, Y. Dong, G. Hu, Multi-core yolk-shell like mesoporous double carbon-coated silicon nanoparticles as anode materials for lithium-ion batteries, Energy Storage Mater. 18 (2019) 165–173.
[10] M. Yang, J. Liu, S. Li, S. Zhang, Y. Wang, C. He, Ultrafast synthesis of graphene nanosheets encapsulated Si nanoparticles via deflagration of energetic materials for lithium-ion batteries, Nano Energy 65 (2019), 104028.
[11] Y. Son, J. Ma, N. Kim, T. Lee, Y. Lee, J. Sung, S.-H. Choi, G. Nam, H. Cho, Y. Yoo, J Cho, Quantification of pseudocapacitive contribution in nanocage-shaped silicon–carbon composite anode, Adv. Energy Mater. 9 (2019), 1803480.
[12] R. Gao, J. Tang, X. Yu, S. Tang, K. Ozawa, T. Sasak, L.-C. Qin, In situ synthesis of MOF-derived carbon shells for silicon anode with improved lithium-ion storage, Nano Energy 70 (2020), 104444.
[13] Y. Zhang, Z. Mu, J. Lai, Y. Chao, Y. Yang, P. Zhou, Y. Li, W. Yang, Z. Xia, S. Guo, MXene/Si@SiO_x@C layer-by-layer superstructure with autoadjustable function for superior stable lithium storage, ACS Nano 13 (2019) 2167–2175.
[14] X. Hui, R. Zhao, P. Zhang, C. Li, C. Wang, L. Yin, Low-temperature reduction strategy synthesized Si/Ti3C2MXene composite anodes for high-performance Li-ion batteries, Adv. Energy Mater. 9 (2019), 1901065.
[15] S. Liu, X. Zhang, P. Yan, R. Cheng, Y. Tang, M. Cui, B. Wang, L. Zhang, X. Wang, Y. Jiang, L. Wang, H. Yu, Dual bond enhanced multidimensional constructed composite silicon anode for high-performance lithium ion batteries, ACS Nano 13 (2019) 8854–8864.
[16] D. Kim, K. Zhang, M. Cho, Y.-M. Kang, Critical design factors for kinetically favorable P-based compounds toward alloying with Na ions for high-power sodium-ion batteries, Energy Environ. Sci. 12 (2019) 1326–1333.
[17] K. Duho, K. Zhang, J.-M. Lim, G.-H. Lee, K. Cho, M. Cho, Y.-M. Kang, GeP3 with soft and tunable bonding nature enabling highly reversible alloying with Na ions, Mater. Today Energy 9 (2018) 126–136.
[18] W. An, B. Gao, S. Wei, B. Xiang, J. Fu, L. Wang, Q. Zhang, P.K. Chu, K. Huo, Scalable synthesis of ant-nest-like bulk porous silicon for high-performance lithium-ion battery anodes, Nat. Commun. 10 (2019) 1447.
[19] S. Guo, H. Li, Y. Lu, Z. Liu, X. Hu, Lattice softening enables highly reversible sodium storage in anti-pulverization Bi–Sb alloy/carbon nanofibers, Energy Storage Mater. 27 (2020) 270–278.
[20] Y. Ren, X. Zhou, J. Tang, J. Ding, S. Chen, J. Zhang, T. Hu, X.-S. Yang, X. Wang, J. Yang, Boron-doped spherical hollow-porous silicon local lattice expansion toward a high-performance lithium-ion-battery anode, Inorg. Chem. 58 (2019) 4592–4599.
[21] S. Huang, L.-Z. Cheong, D. Wang, C. Shen, Nanostructured phosphorus doped silicon/graphite composite as anode for high-performance lithium-ion batteries, ACS Appl. Mater. Interfaces 9 (2017) 23672–23678.
[22] J. Ryu, J.H. Seo, G. Song, K. Choi, D. Hong, C. Wang, H. Lee, J.H. Lee, S. Park, Infinitesimal sulfur fusion yields quasi-metallic bulk silicon for stable and fast energy storage, Nat. Commun. 10 (2019) 2351.
[23] P.R. Abel, A.M. Chockla, Y.-M. Lin, V.C. Holmberg, J.T. Harris, B.A. Korgel, A. Heller, C.B. Mullins, Nanostructured Si(1-x)Gex for tunable thin film lithium-ion battery anodes, ACS Nano 7 (2013) 2249–2257.
[24] D. Duveau, B. Fraisse, F. Cunin, L. Monconduit, Synergistic effects of Ge and Si on the performances and mechanism of the GexSi1–x electrodes for Li ion batteries, Chem. Mater. 27 (2015) 3226–3233.
[25] N. Bensalah, M. Matalkeh, N.K. Mustafa, H. Merabet, Binary Si–Ge alloys as high-capacity anodes for Li-Ion batteries, Phys. Status Solidi A 217 (2020), 1900414.
[26] W. Xiao, J. Zhou, L. Yu, D. Wang, X.W. Lou, Electrolytic formation of crystalline silicon/germanium alloy nanotubes and hollow particles with enhanced lithium-storage properties, Angew. Chem. Int. Ed. 55 (2016) 7427–7431.
[27] J.D. Pack, H.J. Monkhorst, Special points for Brillouin-zone integrations—a reply, Phys. Rev. B 16 (1977) 1748–1749.
[28] G. Kresse, D. Joubert, From ultrasoft pseudopotentials to the projector augmented-wave method, Phys. Rev. B 59 (1999) 1758–1775.
[29] J.R. Rodriguez, Z. Qi, H. Wang, M.Y. Shalaginov, C. Goncalves, M. Kang, K. A. Richardson, J. Guerrero-Sancheze, M.G. Moreno-Armentae, V.G. Pol, Ge2Sb2Se5 glass as high-capacity promising lithium-ion battery anode, Nano Energy 68 (2020), 104326.
[30] G. Bhikshamaiah, M.S. Omar, S.V. Suryanarayana, X-ray determination of thermal lattice expansion of CuSi2 +xP3 (x = 1, 2) at elevated temperatures, Cryst. Res. Technol. 29 (1994) 277–280.
[31] P. Wang, F. Ahmadpour, T. Kolodiazhnyi, A. Kracher, L.M.D. Cranswick, Y. Mozharivskyj, Composition, structure, bonding and thermoelectric properties of "CuT2P3" and "CuT4P3", members of the T1−x(CuP3)x series with T being Si and Ge, Dalton Trans. 39 (2010) 1105–1112.
[32] D.O. Scanlon, A. Walsh, Bandgap engineering of ZnSnP2 for high-efficiency solar cells, Appl. Phys. Lett. 100 (2012), 251911.

[33] M.A. Ryan, M.W. Peterson, D.L. Williamson, J.S. Frey, G.E. Maciel, B.A. Parkinson, Metal site disorder in zinc tin phosphide, J. Mater. Res. 2 (1987) 528–537.
[34] H.H. Heenen, C. Scheurer, K. Reuter, Implications of occupational disorder on ion mobility in Li4Ti5O12 battery materials, Nano Lett. 17 (2017) 3884–3888.
[35] J. Sun, H.-W. Lee, M. Pasta, H. Yuan, G. Zheng, Y. Sun, Y. Li, Y. Cui, A phosphorene–graphene hybrid material as a high-capacity anode for sodium-ion batteries, Nat. Nanotechnol. 10 (2015) 980–985.
[36] W. Li, X. Li, J. Liao, B. Zhao, L. Zhang, L. Huang, G. Liu, A.Z. Guo d, M. Liu, A new family of cation-disordered Zn(Cu)–Si–P compounds as high-performance anodes for next-generation Li-ion batteries, Energy Environ. Sci. 12 (2019) 2286–2297.
[37] Z. Liu, S. Yang, B. Sun, P. Yang, J. Zheng, X. Li, Low-temperature synthesis of honeycomb CuP2@C in molten ZnCl2 salt for high-performance lithium ion batteries, Angew. Chem. Int. Ed. 132 (2020) 1991–1995.
[38] K. Yao, Z. Xu, J. Huang, M. Ma, L. Fu, X. Shen, J. Li, M. Fu, Bundled defect-rich MoS2 for a high-rate and long-life sodium-ion battery: achieving 3D diffusion of sodium ion by vacancies to improve kinetics, Small 15 (2019), 1805405.
[39] Y. Zhou, Y. Yang, G. Hou, D. Yi, B. Zhou, S. Chen, T.D. Lam, F. Yuan, D. Golberg, X. Wang, Stress-relieving defects enable ultra-stable silicon anode for Li-ion storage, Nano Energy 70 (2020), 104568.
[40] J. Zhang, K. Zhang, J. Yang, G.-H. Lee, J. Shin, V.W.-h. Lau, Y.-M. Kang, Bifunctional conducting polymer coated CoP Core–Shell nanowires on carbon paper as a free-standing anode for sodium ion batteries, Adv. Energy Mater. 8 (2018), 1800283.
[41] S. Zhang, Q. Fan, Y. Liu, S. Xi, X. Liu, Z. Wu, J. Hao, W.K. Pang, T. Zhou, Z. Guo, Dehydration-triggered ionic channel engineering in potassium niobate for Li/K-ion storage, Adv. Mater. 32 (2020), 2000380.
[42] C. Teng, D. Xie, J. Wang, Z. Yang, G. Ren, Y. Zhu, Ultrahigh conductive graphene paper based on ball-milling exfoliated graphene, Adv. Funct. Mater. 27 (2017), 1700240.
[43] V. León, A.M. Rodriguez, P. Prieto, M. Prato, E. Vázquez, Exfoliation of graphite with triazine derivatives under ball-milling conditions: preparation of few-layer graphene via selective noncovalent interactions, ACS Nano 8 (2014) 563–571.
[44] Z. Wu, G. Liang, W.K. Pang, T. Zhou, Z. Cheng, W. Zhang, Y. Liu, B. Johannessen, Z. Guo, Coupling topological insulator SnSb2Te4 nanodots with highly doped graphene for high-rate energy storage, Adv. Mater. 32 (2019), 1905632.
[45] Z. Ju, P. Li, G. Ma, Z. Xing, Q. Zhuang, Y. Qian, Few layer nitrogen-doped graphene with highly reversible potassium storage, Energy Storage Mater. 11 (2018) 38–46.
[46] Y. Xu, B. Peng, F.M. Mulder, A high-rate and ultrastable sodium ion anode based on a novel Sn4P3-P@graphene nanocomposite, Adv. Energy Mater. 8 (2018), 1701847.
[47] H. Zhang, P. Zong, M. Chen, H. Jin, Y. Bai, S. Li, F. Ma, H. Xu, K. Lian, In situsynthesis of multilayer carbon matrix decorated with copper particles: enhancing the performance of Si as anode for Li-Ion batteries, ACS Nano 13 (2019) 3054–3062.
[48] Q. Zhang, H. Chen, L. Luo, B. Zhao, H. Luo, X. Han, J. Wang, C. Wang, Y. Yang, T. Zhu, M. Liu, Harnessing the concurrent reaction dynamics in active Si and Ge to achieve high performance lithium-ion batteries, Energy Environ. Sci. 11 (2018) 669–681.
[49] S. Chae, M. Ko, S. Park, N. Kim, J. Ma, J. Cho, Micron-sized Fe–Cu–Si ternary composite anodes for high energy Li-ion batteries, Energy Environ. Sci. 9 (2016) 1251–1257.
[50] H.T. Kwon, C.K. Lee, K.J. Jeon, C.M. Park, Silicon diphosphide: a Si-Based three-dimensional crystalline framework as a high-performance Li-Ion battery anode, ACS Nano 10 (2016) 5701–5709.
[51] D. Duveau, S.S. Israel, J. Fullenwarth, F. Cunin, L. Monconduit, Pioneer study of SiP2 as negative electrode for Li- and Na-ion batteries, J. Mater. Chem. A 4 (2016) 3228–3232.
[52] J. Zhu, Q. Wu, J. Key, M. Wu, P.K. Shen, Self-assembled superstructure of carbon-wrapped, single-crystalline Cu3P porous nanosheets: One-step synthesis and enhanced Li-ion battery anode performance, Energy Storage Mater. 15 (2018) 75–81.
[53] M. Cristian Stan, R. Klöpsch, A. Bhaskar, J. Li, S. Passerini, M. Winter, Cu3P binary phosphide: synthesis via a wet mechanochemical method and electrochemical behavior as negative electrode material for lithium-ion batteries, Adv. Energy Mater. 3 (2013) 231–238.
[54] S. Liu, X. He, J. Zhu, L. Xu, J. Tong, Cu3P/RGO nanocomposite as a new anode for lithium-ion batteries, Sci. Rep. 6 (2016) 35189.
[55] Y. Domi, H. Usui, M. Shimizu, Y. Kakimoto, H. Sakaguchi, Effect of phosphorus-doping on electrochemical performance of silicon negative electrodes in lithium-ion batteries, ACS Appl. Mater. Interfaces 8 (2016) 7125–7132.
[56] S.W. Kim, J.H. Yun, B. Son, Y.G. Lee, K.M. Kim, Y.M. Lee, K.Y. Cho, Graphite/silicon hybrid electrodes using a 3D current collector for flexible batteries, Adv. Mater. 26 (2014) 2977–2982.
[57] R. Reinhold, D. Mikhailova, T. Gemming, A.B. Missyul, C. Nowka, S. Kaskel, L. Giebeler, Silicon monophosphide as a possible lithium battery anode material, J. Mater. Chem. A 6 (2018) 19974–19978.
[58] H. Song, H. Wang, Z. Lin, X. Jiang, L. Yu, J. Xu, Z. Yu, X. Zhang, Y. Liu, P. He, L. Pan, Y. Shi, H. Zhou, K. Chen, Highly connected silicon-copper alloy mixture nanotubes as high-rate and durable anode materials for lithium-ion batteries, Adv. Funct. Mater. 26 (2016) 524–531.
[59] H. Song, S. Wang, X. Song, H. Yang, G. Du, L. Yu, J. Xu, P. He, H. Zhou, K. Chen, A bottom-up synthetic hierarchical buffer structure of copper silicon nanowire hybrids as ultra-stable and high-rate lithium-ion battery anodes, J. Mater. Chem. A 6 (2018) 7877–7886.
[60] S.O. Kim, A. Manthiram, Phosphorus-rich CuP2 embedded in carbon matrix as a high-performance anode for lithium-ion batteries, ACS Appl. Mater. Interfaces 9 (2017) 16221–16227.
[61] J. Li, X. Li, P. Liu, X. Zhu, R. Nauman Ali, H. Naz, Y. Yu, B. Xiang, Self-supporting hybrid fiber mats of Cu3P–Co2P/N–C endowed with enhanced lithium/sodium ions storage performances, ACS Appl. Mater. Interfaces 11 (2019) 11442–11450.
[62] S. Huang, L. Zhang, L. Liu, L. Liu, J. Li, H. Hu, J. Wang, F. Ding, O.G. Schmidt, Rationally engineered amorphous TiOx/Si/TiOx nanomembrane as an anode material for high energy lithium ion battery, Energy Storage Mater. 12 (2018) 23–29.
[63] S. Ni, B. Zheng, J. Liu, D. Chao, X. Yang, Z. Shen, J. Zhao, Self-adaptive electrochemical reconstruction boosted exceptional Li+ion storage in a Cu3P@C anode, J. Mater. Chem. A 6 (2018) 18821–18826.
[64] S. Chen, L. Shen, P.A. van Aken, J. Maier, Y. Yu, Dual-functionalized double carbon shells coated silicon nanoparticles for high performance lithium-ion batteries, Adv. Mater. 29 (2017), 1605650.
[65] W.-C. Chang, K.-W. Tseng, H.-Y. Tuan, Solution synthesis of iodine-doped red phosphorus nanoparticles for lithium-ion battery anodes, Nano Lett. 17 (2017) 1240–1247.
[66] S. Zhang, Y. Zheng, X. Huang, J. Hong, B. Cao, J. Hao, Q. Fan, T. Zhou, Z. Guo, Structural engineering of hierarchical micro-nanostructured Ge–C framework by controlling the nucleation for ultralong-life Li storage, Adv. Energy Mater. 9 (2019), 1900081.
[67] Y. Wang, S. Luo, M. Chen, L. Wu, Uniformly confined germanium quantum dots in 3D ordered porous carbon framework for high-performance Li-ion battery, Adv. Funct. Mater. 30 (2020), 2000373.
[68] M. Shang, X. Chen, B. Li, J. Niu, A fast charge/discharge and wide-temperature battery with a germanium oxide layer on a Ti3C2MXene matrix as anode, ACS Nano 14 (2020) 3678–3686.

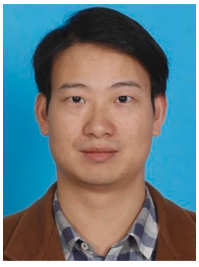

Wenwu Li received his Ph.D. degree in Materials Science and Engineering from Huazhong University of Science and Technology in 2016. Then, he worked as an associate professor in the School of Materials and Energy, Guangdong University of Technology, Guangzhou, China, and a visiting scholar in the School of Materials Science and Engineering, Georgia Institute of Technology, USA, 2018–2019. His current research interests are focused on designing novel P-based anode materials with high-security for metal ion batteries and uncovering the fundamental structure-performance relationships behind high metal ion storage performance and the mechanisms involved.

Qibin Ma received his B.S. degree from the Shaoguan College in 2019. Now he is a Master's degree candidate of the School of Materials and Energy, Guangdong University of Technology (GDUT). His research is concentrated on developing high-performance anode materials for rechargeable alkali metal ion batteries.

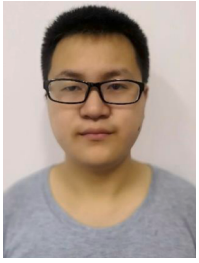

Pengfei Shen received his B.S. degree from the East China University of Technology in 2018. Now he is a Master's degree candidate of the School of Materials and Energy, Guangdong University of Technology (GDUT). His research is concentrated on developing high-performance anode materials for rechargeable alkali metal ion batteries.

Yucun Zhou received his B.E. degree in Inorganic Non-metallic Materials Engineering from Shandong University, China in 2010 and earned his Ph.D. degree in Materials Physics and Chemistry from Shanghai Institute of Ceramics, Chinese Academy of Sciences in 2015. He is currently a postdoctoral research associate in the School of Materials Science and Engineering at Georgia Institute of Technology. His research interests include solid oxide fuel cells, lithium-sulfur batteries, redox flow batteries and solid-state batteries. He is currently focusing on the development of electrodes and catalysts for reversible solid oxide fuel cells.

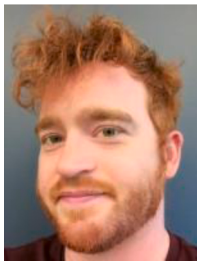

Luke Soule received his B.S. degree of Materials Engineering Senior from New Mexico Institute of Mining and Technology. Now he is a Ph.D. candidate at Georgia Tech. His current and future research interests lie in renewable energy research and the development and implementation of sustainable materials and materials processing.

Yunyong Li is a professor of School of Material and Energy in Guangdong University of Technology. He received his Ph.D. degree under the supervision of Prof. Pei Kang Shen in School of Physics and Engineering, Sun Yat-sen University in 2014. He received his M.S. in College of Chemistry and Chemical Engineering, Hunan Normal University in 2011. He currently research interests mainly focus on the two-dimensional energy storage materials in the field of advanced energy storage devices such as lithium/sodium ion batteries, supercapacitors, lithium-sulfur batteries, etc.

Yanxue Wu is currently the micro-area analysis section chief of Analysis and Test Center, Guangdong University of Technology. He received his Ph.D. degree in geochemistry from the Institute of Geochemistry, Chinese Academy of Sciences. His main research interests are space resource utilization and electron microscopy methods for the analysis in materials science (such as energy storage materials and solid-state batteries).

Haiyan Zhang is a professor and dean of School of Material and Energy in Guangdong University of Technology. She received her B.S. and Ph.D. degree from Sun Yat-sen University in 1982 and 1998, respectively. She has published more than 80 research papers. Her research interests include the synthesis of nano-carbon materials (carbon nanotube, carbon coated metal nanoparticles, graphene) and their applications in energy materials.

Meilin Liu is a B. Mifflin Hood Chair, Regents' Professor, Associate Chair of Materials Science and Engineering, and Co-Director of the Center for Innovative Fuel Cell and Battery Technologies at Georgia Institute of Technology, USA. He received his B.S. from South China University of Technology and both M.S. and Ph.D. from University of California at Berkeley. His research interests include in-situ/operando characterization and multi-scale modeling of charge and mass transfer along surfaces, across interfaces, and in membranes, thin films, and nanostructured electrodes, aiming at achieving rational design of materials and structures with unique functionalities for efficient energy storage and conversion.